Post-Print of an Accepted Manuscript on the Laboratory of Turbulent Flows Website

Complete citation:

The Accepted Manuscript begins on the next page.

Near-wall motion of inertial particles in a drag-reduced non-Newtonian turbulent flow

M. Ebrahimian · R. S. Sanders ·

S. Ghaemi

Abstract The kinematics of inertial particles suspended in the near-wall region of Newtonian and non-Newtonian turbulent channel flows was experimentally investigated. The non-Newtonian fluid was a homogeneous solution of 90 part per million of a polyacrylamide polymer in water with 66% drag reduction. All the experiments were performed at the same volumetric flow rate with Reynolds number of 34,300 based on bulk velocity, channel height, and the kinematic viscosity of water. The inertial particles were 250 µm glass beads with St of 35 (in water) at a volumetric concentration of 0.05%. A time-resolved two-dimensional particle tracking velocimetry was used to record particle images at acquisition frequency of 17.6 kHz and detect trajectory of flow tracers and the glass beads. The recorded data was processed using a two-

M. Ebrahimian
Department of Mechanical Engineering, University of Alberta, Edmonton, Alberta T6G 1H9, Canada

R. S. Sanders
Department of Chemical and Materials Engineering, University of Alberta, Edmonton, Alberta T6G 1H9, Canada

S. Ghaemi (Corresponding author)
Department of Mechanical Engineering, University of Alberta, Edmonton, Alberta T6G 1H9, Canada
E-mail: ghaemi@ualberta.ca

dimensional particle tracking algorithm to obtain the Lagrangian kinematics of the beads. The comparison between laden flows of water and polymer solution showed reduction of number density of the beads and their momentum in the vicinity of the wall in the polymeric flow. The polymer solution remarkably reduced the wall-normal and shear Reynolds stresses of the beads, but had a negligible effect on their streamwise Reynolds stress. The wall-normal fluctuation of the beads reduced in the polymeric flow and their trajectories became parallel with the channel wall. Results also showed that the ejection and sweep motions were not the major mechanism for wall-normal distribution of the beads in the polymeric flow. Outcomes suggest that drag-reducing polymer solutions have the potential of reducing erosive wear in particle-laden pipelines.

Keywords non-Newtonian turbulent flow · particle-laden flow · particle tracking velocimetry · polymer drag reduction

1 Introduction

Adding solid particles to a fluid increases the apparent viscosity of the mixture (Einstein 1956; Senapati et al 2010) and causes larger pressure drop in internal flows (Wasp et al 1977; Kaushal et al 2005), requiring higher power to pump the mixture. In addition, the kinetic energy that the particles absorb from the carrier phase dissipates through their collision with the pipe wall (Joseph et al 2001) and other particles (Morgado and Oppenheim 1997). The higher pumping power and erosive wear due to particle-wall collision are among the important remaining challenges of slurry pipelines (Karabelas 1978; Kosel 1992; Gupta et al 1995). Polymers with large molecular weight are well known to be effective in reducing drag and pumping power in unladen turbulent liquid flows (Virk et al 1970; Luchik and Tiederman 1988; Warholic

et al 1999). However, to the authors' knowledge, the effect of polymer drag reducers on the kinematics of particles in non-Newtonian turbulent flows with viscoelastic properties has not been investigated.

Previous studies of particle motion in non-Newtonian flows have mostly investigated individual particles released in quiescent fluids or laminar flows at small Reynolds numbers (D'Avino and Maffettone 2015; McKinley 2002; Chhabra 2006; Mishra S 2012; Li et al 2015). The viscoelastic properties of the fluid was typically characterized in terms of Deborah number (De, the ratio of fluid relaxation time to the flow time-scale) and Weissenberg number (Wi) which is the ratio of the elastic forces to the viscous forces of the fluid (D'Avino and Maffettone 2015). In general, the influence of these parameters on the kinematics and dynamics of particles was investigated based on the terminal settling velocity, Stokes number (St, the ratio of the particle relaxation time to the flow time-scale), translation, rotation, and lift and drag force of individual solid particles at low Reynolds number (Re).

In the case of non-Newtonian flows with a large number of suspended particles, previous investigations have mostly focused on distribution of particles in terms of their migration, alignment, and clustering in the low Re regime, where inertia is negligible and fluid elasticity is dominant (D'Avino and Maffettone 2015). At low Re channel flows, Karnis and Mason (1966) reported particle migration toward the centerline for viscoelastic fluids with constant viscosity while Gauthier et al (1971) reported particle migration toward the walls for shear-thinning fluids. The alignment of particles at the channel centreline (known as "focusing") has been observed in microchannels at $0 < Re < 1$ and $0 < Wi < 250$ (Yang et al 2011; Kang et al 2013; Seo et al 2014), and even at higher Re of about 2000 for $Wi \approx 200$ (Lim et al 2014). In spite of the great number of studies on particle motion in laminar and transitional non-

Newtonian flows, the motion of particles in turbulent non-Newtonian flows with stronger inertial effects has not been investigated yet.

In Newtonian turbulent wall flows, the interaction of near-wall turbulent structures and particles significantly affects the kinematics, dispersion, and clustering of the particles. Due to gravity, inertial particles tend to proceed toward the lower wall in horizontal flows. The particles move from the outer layer into the inner layer where they are either farther transported toward the wall by sweep motions (Sumer and Deigaard 1981; Marchioli and Soldati 2002), or sent back to the outer layer by ejection motions of the liquid phase (Marchioli and Soldati 2002; Kiger and Pan 2002; Soldati and Marchioli 2009). The particles that are carried by the sweep motions toward the wall may collide with the wall and bounce off to higher layers if they have enough momentum (Soldati 2005); otherwise they get trapped in low-speed streaks (Pedinotti et al 1992; Kaftori et al 1995a,b). Inertial particles which are smaller than the Kolmogorov scale typically do not concentrate in high-speed streaks because of the rotational motion of these turbulent structures (Pedinotti et al 1992). The small particles often cluster in low-speed streaks, and remain there until they are propelled away from the wall by strong enough ejection motions (Marchioli and Soldati 2002; Soldati 2005). Smaller particles with small St usually stay in the vicinity of the wall for a shorter time since they can be transported away from the wall by weaker ejection motions (Soldati 2005). Therefore, in turbulent Newtonian flows, sweep and ejection motions are the main turbulent structures which disperse the particles, depending on their size and St.

In a non-Newtonian flow, the near-wall turbulent structures are modified due to the fluid's rheology (Warholic et al 2001). The addition of drag reducing polymers decreases turbulent kinetic energy and Reynolds shear stress (Warholic et al 1999), thickens and stabilizes the low/high speed streaks (White et al 2004; White and Mungal 2008), and increases their spanwise

spacing (White et al 2004). Polymer additives also attenuate the near-wall quasi-streamwise vortices, reduce their number (Dubief et al 2004; Kim et al 2007; White and Mungal 2008), and make them longer (Kim et al 2007). The ejection and sweep motions also become weaker and less frequent (Kim et al 2007; Corredor et al 2015). In general, this suppression of turbulent structures disrupts the regeneration cycle of wall turbulence (Karniadakis and Choi 2003; Dubief et al 2004). Since fluid forces have a significant effect on kinematics and dispersion of suspended particles, changing turbulent structures by polymer additives is expected to also affect particles motion.

In light of the literature reviewed, the objective of this investigation is to experimentally characterize the kinematics of inertial particles and their dispersion in a drag-reduced turbulent channel flow of a polymer solution. To achieve this objective, trajectories of inertial solid particles is determined using a time-resolved two-dimensional particle tracking velocimetry (PTV) in the turbulent flow of water (Newtonian) and the polymer solution (non-Newtonian). The particle trajectories are used to investigate the influence of the polymer additive on wall-normal distribution, streamwise and wall-normal velocities, Reynolds stresses, and the transport angle of the particles in near-wall region. The influence of the polymer additive on the ejection and sweep motions of the particles was investigated by applying a quadrant analysis. The experimental setup and the PTV processing algorithm of this study are detailed in Section 2. The accuracy of the measurement system is evaluated in Section 3.1 by comparing the measurements in the unladen Newtonian flow with the literature. The motion of the particles in Newtonian and non-Newtonian flows are investigated in Section 3.2.
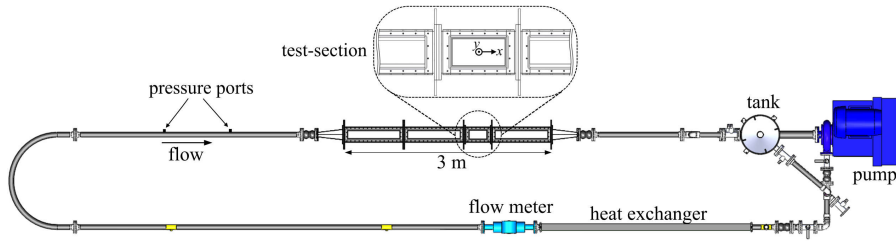
Fig. 1: Top-view of the flow-loop equipped with a transparent test-section, a Coriolis flow-meter, a centrifugal pump, and a heat exchanger to keep the temperature constant during the experiments. The zoomed-in view shows the test-section and the coordinate system. The flow was in the x-direction. The origin of the y-axis is on the bottom wall and its positive direction is toward the top wall. The high-speed PTV system captured the images of the $x - y$ plane illuminated by a laser-sheet.

2 Experimental setup

Experiments were carried out in a closed horizontal flow-loop equipped with a test section that has a rectangular cross section, as seen in Fig. 1. This facility was used to investigate four turbulent flows: unladen water flow (Newtonian); unladen polymeric flow (non-Newtonian); particle-laden water flow (Newtonian); and particle-laden polymeric flow (non-Newtonian). The specifications of the flow facility, the PTV system, the unladen flow, and the particle-laden flow are detailed in the following sections.

2.1 Flow facility

Measurements were carried out at the test-section of the channel which has a rectangular cross-section with dimensions of $(W \times 2H) = 120 \times 15$ mm^2 and hydraulic diameter of the 26.7 mm. The measurement location was $220H$ downstream of the channel entrance, ensuring a fully developed turbulent flow. The glass walls of the test-section provided optical access for illumination and imaging. Two gradual transition sections with a length of 30 cm were used

at the ends of the channel to connect it to 2-inch diameter pipes. The flow
was circulated in the flow-loop by a centrifugal pump (GIW Inc.). To reduce
vibration induced by the pump, the channel was isolated from the flow loop
by two rubber joints. A Coriolis flow meter (Micro Motion F-Series, Emerson
Industries) with the mass flow accuracy of 0.2% was used to measure flow
rate and temperature of the flow. A double-pipe heat exchanger was used to
keep the temperature constant at 25°C. The experiments were performed at a
constant mass flow rate of 3.66 kg/s equivalent to Newtonian Re_{H0} of 34,300,
based on the channel height, bulk velocity across the channel ($U_\mathrm{b} = 2.04$ m/s),
and viscosity of water. The pressure drop between two pressure ports with 1
m distance (see Fig. 1) was measured using a Validyne DP-15 pressure trans-
ducer with 0.2 psi diaphragm and accuracy of 0.25% of the full-scale pressure.
The demodulated signal of the pressure transducer was acquired by a data
acquisition card with 12-bit resolution (National Instruments NI-9201 DAQ)
at 100 Hz frequency. The pressure measurement was used to determine the
drag reduction (DR) of the polymer solution. The drag reduction percentage
($DR\%$) is calculated as $DR\% = (1 - \Delta P_\mathrm{p}/\Delta P_\mathrm{w}) \times 100$, where ΔP_w and ΔP_p
are pressure drops between two pressure ports for water and polymeric flows,
respectively. The center of the coordinate system was located at the mid-span
of the bottom wall, as showed in Fig. 1. The y-axis pointed in the wall-normal
direction from the bottom wall to the top wall and the flow was in the x
direction.

2.2 Unladen turbulent flow

The unladen Newtonian and non-Newtonian experiments were carried out us-
ing tap water. For the polymeric flow experiments, a 90 ppm solution of an
anionic polyacrylamide (APAM) with high molecular weight and medium an-

ionic charge density, which is called Superfloc (SF) A-125V (Kemira Chemi-
cals Inc.), was used. The polymer powder was weighed using a scale (Mettler
Toledo, AB104-S) with 0.1 mg resolution to prepare a 90 ppm SF solution in
water. This polymer concentration was chosen to obtain a high drag reduc-
tion with small mechanical degradation due to shear. Based on the pressure
measurement at the mass flow rate of 3.66 kg/s, the average $DR\%$ was $\approx 66\%$
in 30 minutes, which is considered as high drag reduction regime (Warholic
et al 1999), and its degradation was $\approx 3.7\%$. The polymer powder was grad-
ually added to 210 liters of water in a mixing tank while a mixer (Lightnin
Labmaster, L5U10F) was operating at 75 rpm. The mixer was equipped with
a low-shear three-bladed marine impeller with a diameter of 250 mm. The
impeller was located at about half depth of the solution in the tank as it is
recommended by Tatterson (1991) and the mixture was mixed for 2 hours
(Rowin et al 2018). The difference between the densities of the water and SF
solution was negligible.

A rheometer (RheolabQC, Anton Paar USA, Inc.) equipped with a double-
gap cylinder was used to measure the dynamic shear viscosity (μ) of the poly-
mer solution. Due to the small gap between the cylinders, the double-gap
cylinder system can measure viscosity at high shear rate ($\dot{\gamma}$) in a laminar flow
by avoiding transition to turbulence, which reduces the measurement accu-
racy (Taylor 1923). The shear stress (τ) applied to the polymer solution at
different $\dot{\gamma}$ is presented on the left vertical axis of Fig. 2 along with the asso-
ciated μ shown on the right vertical axis of the plot. As this figure shows, the
slope of τ versus $\dot{\gamma}$ gradually decreases up to about $\dot{\gamma} = 200$, which indicates
a shear-thinning behavior of power-law fluids (Hatschek 1939). This behavior
can be described by Ostwald-de Waele model (Hatschek 1939), $\tau = K(\dot{\gamma})^n$,
where K and n are the flow consistency and behavior indices, respectively.
These indices are estimated by fitting the Ostwald–de Waele model to the

measured τ, as shown in Fig. 2. For the polymer solution used in this study $K = 8.05 \times 10^{-3}$ (Pa.s^n) and $n = 0.766$. In case of higher $\dot{\gamma}$, the associated τ can be extrapolated using the fitted Ostwald–de Waele model.

The average dynamic viscosity at the wall (μ_{w}) in turbulent flows can be estimated as $\mu_{\mathrm{w}} = \tau_{\mathrm{w}}/\dot{\gamma}_{\mathrm{w}}$, where τ_{w} and $\dot{\gamma}_{\mathrm{w}}$ are the average shear stress and shear rate at the wall, respectively. Here, the subscript w refers to parameters estimated at the wall. The $\dot{\gamma}_{\mathrm{w}}$ of the polymeric flow was determined from the wall-normal velocity profile measured by PTV, as detailed later in Section 3.1. The wall shear stress associated with this $\dot{\gamma}_{\mathrm{w}}$ was determined based on the Ostwald–de Waele model. Having $\dot{\gamma}_{\mathrm{w}}$ and τ_{w}, the associated kinematic viscosity at the wall (ν_{w}) was estimated for the polymeric flow and is shown in Table 1. The viscosity of a power-law fluid in a channel flow is at its minimum at the wall where average $\dot{\gamma}$ is maximum, and at its maximum at the centerline of the channel, where average $\dot{\gamma}$ is a minimum. The friction velocity (u_τ) and wall unit (λ) were also estimated from the PTV measurement and are presented in Table 1. The time scale of turbulent flows was estimated at the wall as $t_{\mathrm{f}} = \nu_{\mathrm{w}}/u_\tau^2$ and the friction Reynolds number was determined as $Re_\tau = u_\tau H/\nu_{\mathrm{w}}$.

Table 1: The inner scaling of the unladen turbulent water and polymeric flows including shear rate ($\dot{\gamma}_{\mathrm{w}}$), kinematic viscosity ($\nu_{\mathrm{w}}$), friction velocity ($u_\tau$), wall-unit ($\lambda$), inner time scale ($t_{\mathrm{f}}$), and the friction Reynolds number (Re_τ). The shear rate at the wall and inner scaling were calculated using the mean velocity profiles from PTV.

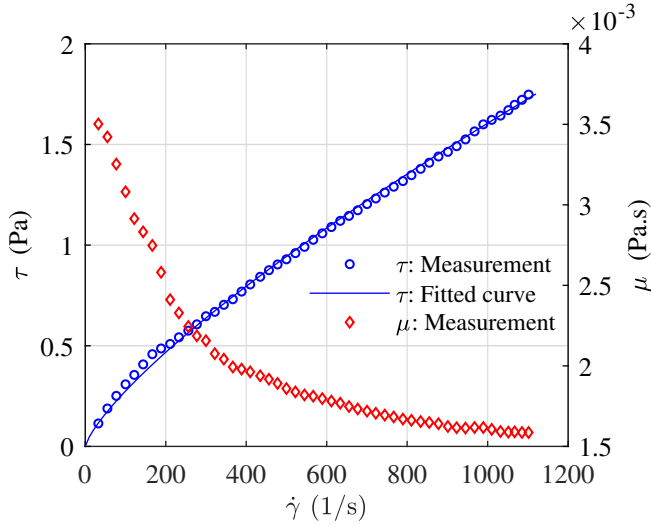| Fluid	$\dot{\gamma}_{\mathrm{w}}$ $1/s$	ν_{w} $\times 10^6 \mathrm{m}^2\mathrm{s}$	u_τ m/s	λ μm	t_{f} μs	Re_τ
water	11500	0.893	0.101	8.9	89	840
SF solution	2260	1.330	0.054	24.3	443	309

Fig. 2: The measured τ and μ of the polymer solution at different $\dot{\gamma}$. The solid line shows the fitted curve on τ profile based on the Ostwald—de Waele model.

2.3 Particle-laden turbulent flow

The particle-laden flows consisted of 250 μm glass beads with density of 2608±2.6 kg/m³ at volumetric concentration of 0.05% suspended in water (Newtonian) and in the 90 ppm SF solution (non-Newtonian). The standard deviation of the diameter of the detected beads was about 25 μm. Visual inspection of images showed that the centrifugal pump did not break the glass beads, and the beads kept their shape and size during the experiments. The effect of glass beads on the apparent viscosity of the mixture is negligible considering their low volumetric concentration (Stickel and Powell 2005). The St of the beads is estimated as the ratio of their relaxation time $t_{\mathrm{p}} = (\rho_{\mathrm{p}} - \rho_{\mathrm{f}})d_{\mathrm{p}}^2/(18\mu)f_{\mathrm{d}}$ to the turbulent time scale of the flow. Here d_{p}, ρ_{p}, ρ_{f}, and μ are the mean diameter of the particles (i.e. glass beads), density of the beads, density of the carrier phase, and the dynamic viscosity of the carrier phase, respectively. The coefficient $f_{\mathrm{d}} = 1 + 0.15Re_{\mathrm{p}}^{0.687}$ is a drag correction factor to compensate for the deviation from the Stokes regime (Clift and Gauvin 1971).

Based on their terminal settling velocity, $V_{\mathrm{t}} = (4gd_{\mathrm{p}}(\rho_{\mathrm{p}} - \rho_{\mathrm{f}})/(3\rho_{\mathrm{f}})C_{\mathrm{d}})^{0.5}$, the Reynolds number of the glass beads is determined as $Re_{\mathrm{p}} = d_{\mathrm{p}}V_{\mathrm{t}}/\nu$, where ν is the kinematic shear viscosity of fluid, g is the gravitational acceleration, and C_{d} is the drag coefficient of the beads which is determined based on Re_{p}. In the Newtonian flow ν does not depend on $\dot{\gamma}$. Therefore, for the laden water flow, the defined Re_{p} and t_{p} are constant in different wall-normal locations (y) and are presented in Table 2 for the beads suspended in water. The St of these beads is also presented in the table based on the turbulent time scale of the flow at the wall, t_{f}.

The drag coefficient of a spherical particle in a power-law fluid is typically estimated based on $Re_{\mathrm{pl}} = \rho_{\mathrm{f}}V_{\mathrm{t}}^{(2-n)}d_{\mathrm{p}}^{n}/K$, where Re_{pl} is the particle's Reynolds number in power-law fluid (Chhabra and Richardson 1999). Based on this estimation, V_{t} of glass beads in the SF solution is 0.0152 m/s and their Re_{pl} is 1.22. However, this procedure does not consider fluid elasticity and may overestimate V_{t} (Arnipally and Kuru 2017). To determine V_{t} of the beads in the SF solution, a glass bead was released in the middle of a $8 \times 8 \times 8$ cm^3 container filled with the 90 ppm SF solution. The bead's velocity was measured in a 5×5 mm^2 field-of-view, which was 20 mm away from the bottom of the container. The images were recorded at digital resolution of 2.95 µm/pix at 2 kHz frequency. The uncertainty is 6×10^{-4} m/s based on 0.1 pix uncertainty in detection of bead location. A negligible variation of bead's velocity was observed within the field-of-view, which indicates that the bead has reached its terminal settling velocity. The average V_{t} from five tests was 0.011 m/s with standard deviation of 0.002 m/s, which resulted in Re_{p} of 2.07 based on μ_{w}. The values of V_{t} and Re_{p} are presented in Table 2 along with the associated t_{p} and St for the glass beads in the polymeric flow based on μ_{w}. At $y/H = 0.008$, accounting for the corresponding shear viscosity, the values

of Re_p and t_p are 2.03 and 3.35 ms, respectively. At $y/H = 0.63$, Re_p and t_p variables decrease to 0.77 and 1.39 ms, respectively.

The balance between gravitational settling of the glass beads and their suspension by turbulence is characterized by the Rouse number, $R = V_\mathrm{t}/(\kappa u_\tau)$ (Rouse 1937). The Rouse number for the glass beads in water ($\kappa = 0.41$) and polymeric flows ($\kappa = 0.08$) is presented in Table 2. The glass beads in the polymeric flow have a larger R than in water flow, showing reduction of turbulence contribution to bead suspension. The pressure measurement in the bead-laden polymeric flow experiment showed $DR\%$ of about 61% which is 5% less than the unladen polymeric flow.

Table 2: Properties of the inertial beads in the bead-laden experiments including terminal settling velocity (V_t), particle Reynolds number (Re_p), particle relaxation time (t_p), Stokes number (St), and Rouse number (R). The Re_p, t_p, and St in the SF solution are determined based on the viscosity at the wall.

Fluid	V_t m/s	Re_p	t_p ms	St	R
water	0.059	16.47	3.11	35.5	1.42
SF solution	0.011	2.07	3.39	7.8	2.34

2.4 Time-resolved PTV

To record the Lagrangian trajectory of the glass beads and measure their velocity in the turbulent channel flow a high-speed two-dimensional PTV was applied. The measurement system included a dual-cavity Nd:YLF laser (DM20-527, Photonics Industries) with a wavelength of 527 nm. Each cavity of the laser has a maximum energy of 20 mJ per pulse (at 1 kHz). The laser illuminated a field-of-view of 12.5×4.8 mm^2. A combination of cylindrical and spherical lenses was used to form a laser sheet with about 1 mm thickness. The

laser sheet was directed from the bottom window and covered a streamwise-wall-normal plane $(x - y)$ in the mid-span of the channel. The PTV images were recorded by a CMOS high-speed camera (Phantom v611) with pixel size of 20×20 μm^2 operated at a cropped sensor size of 896×348 pix. A Sigma SLR objective lens with a focal length of $f = 105$ mm at aperture size of $f/8$ was used to image at a magnification of 1.42, digital resolution of 0.014 mm/pix, and the depth-of-field of 0.5 mm. A programmable timing unit (PTU X, LaVision GmbH) controlled by DaVis 8.4 (LaVision GmbH) was used to synchronize the laser with the camera.

Time-resolved images were recorded at an acquisition rate of 17.6 kHz with each laser cavity operating at 8.8 kHz. The unladen flow measurements were implemented by tracking 2 μm silver-coated tracers (SG02S40 Potters Industries) which were added to the flow. These tracers had a density of 3.6 g/cm^3 and relaxation time of $\approx$0.65 μs in the Newtonian experiments. The tracers had an image size of 3 pix and their number density in the frames was about 0.03 tracer per pixel, equivalent to 153 tracers/mm^2. The maximum displacement of the tracers in unladen flow measurement was about 10 pix between two consecutive frames. The 250 μm glass beads in laden flow measurements had an image diameter of about 18 pix, with a maximum displacement similar to that of the tracers. In the bead-laden flows glass beads were separated from the tracers based on their size. The specifications of PTV setup are detailed in Table 3.

To remove the background intensity caused by reflection of the laser sheet, and improve the signal-to-noise ratio of the images, the minimum intensity of the ensemble of images was subtracted from each image. The resulting images were multiplied by a constant to reach the maximum digital threshold and then they were normalized by the average intensity of the ensemble. The signal-to-noise ratio was also improved by subtracting the sliding minimum intensity

Table 3: The specifications of the PTV system.

Field-of-view	12.5×4.8 mm^2
Magnification	1.43
Digital resolution	0.014 mm/pix
Depth of field	0.5 mm
Image size of tracers	3 pix
Image size of beads	18 pix
Image acquisition frequency	17.6 kHz

within a kernel size of 3 pixels followed by normalization using local average intensity within a kernel of 10 pixels. A Gaussian filter with a kernel size of 3×3 pixel was also applied (Kähler et al 2012). The trajectory of tracers in unladen and bead-laden experiments were processed using time-resolved PTV in Davis 8.4 (LaVision GmbH). The maximum change in displacement was limited to 5 pixel and the maximum relative velocity change to 50% between two temporally consecutive velocity vectors.

The trajectories of the glass beads in the two-phase flow measurements were detected using a particle tracking algorithm developed in MATLAB (Math-Works Inc.). In the first step, the location of the beads in all the recorded frames was detected using circle Hough transforms (Yuen et al 1990; Atherton and Kerbyson 1999) and an interrogation window was defined around each bead. Based on the mean velocity profile, the algorithm predicted the location of each bead in the next image frame. Another interrogation window was defined around the predicted location and the precise location of the bead was determined from the correlation peak between the two interrogation windows. This process was continued by detecting and tracking beads in the subsequent frames to form time resolved tracks (Ohmi and Li 2000).

The time-resolved streamwise and wall-normal instantaneous velocities (U and V) of the tracers and the beads were obtained by applying a quadratic

regression fit with temporal kernel (t_k) of 1.7 ms (27 consecutive frames) on their trajectories. For consistency of the estimations, trajectories shorter than 1.7 ms were discarded. The kernel size (t_k) was selected by evaluating the standard deviation of the streamwise acceleration (a_x) in unladen water flow following the method presented by Voth et al (2002) and Gerashchenko et al (2008). The variation of a_x at $y/H = 0.017$ (peak location of the streamwise Reynolds stress) with the temporal kernel is presented in Fig. 3. It is observed that the estimated a_x deviates from the fitted exponential function at $t_k \approx$ 1.7 ms. This deviation indicates that the noise in estimation of a_x rapidly increases for shorter temporal kernels. Therefore, t_k of 1.7 ms was selected as the optimum kernel size.

More than 1.7×10^6 trajectories longer than 1.7 ms were detected in 40,000 images recorded for unladen water and polymeric flows. From 57,000 images recorded for bead-laden water flow experiments, more than 46,000 bead trajectories were detected while 18,000 of them were longer than 1.7 ms. For the bead-laden polymeric flow 57,000 images were also recorded, about 14,000 trajectories were detected and more than 2,000 of them were longer than 1.7 ms. As will be discussed in Section 3.2.1, the smaller number of bead trajectories in the near-wall region of polymeric bead-laden flow is due to more uniform distribution of beads in the wall-normal direction, reducing their near-wall concentration. Samples of the beads' trajectories in water and polymeric flows detected by the developed algorithm are presented in Fig. 4.
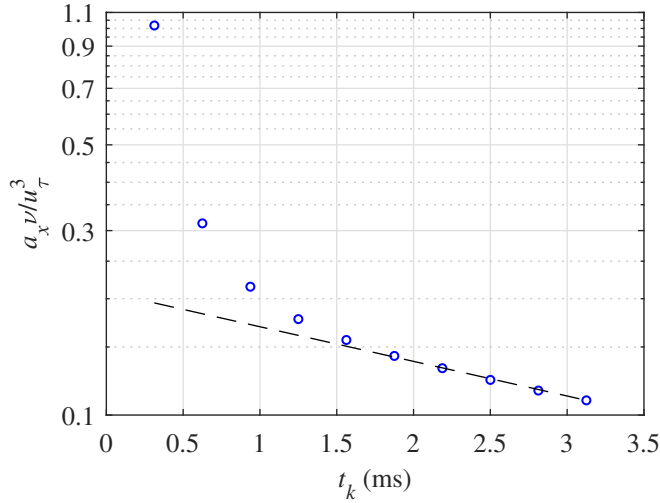
Fig. 3: The variation of normalized a_x of the unladen water flow at $y/H = 0.017$ as a function of t_k (symbols). The dashed straight line shows the fitted exponential function based on the method presented by Voth et al (2002).

3 Results and discussion

In this section, first the uncertainty of the PTV is evaluated by comparing the PTV measurement in water with the DNS of Hoyas and Jiménez (2008) at $Re_\tau = 934$. To the authors' knowledge, this is the closest Re_τ to the experimental conditions of this study at $Re_\tau = 840$. Next, the velocity field and turbulence statistics of the unladen water and polymeric flows are compared. Finally, the average velocity and Reynolds stresses of the beads in water and polymeric flows are scrutinized. The wall-normal distance, averaged velocities, and the Reynolds stresses presented in this section are normalized by either the inner scaling of the unladen water flow (presented with subscript "0") or inner scaling of the corresponding unladen counterpart (presented without subscript "0"). The random errors of the velocity statistics of unladen and bead-laden flows are reported in the Appendix.
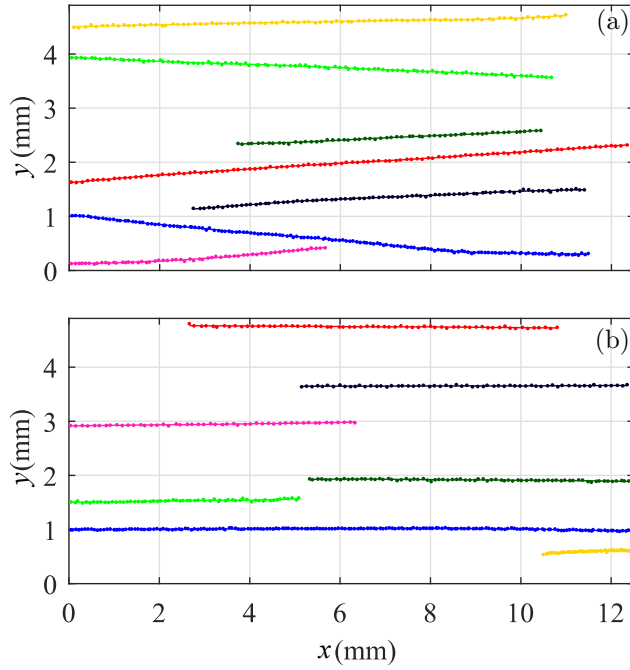
Fig. 4: Samples of beads trajectory in (a) water and (b) polymeric flows. These trajectories were detected using the PTV algorithm. Symbols show the detected glass bead positions and the lines show the quadratic fit with the temporal kernel of 1.7 ms.

1   3.1 Unladen turbulent flow

2   The velcoity statistics of unladen water and polymeric flows are presented

3   in this section. The bin size for averaging PTV data of the unladen flows is

4   equal to λ of unladen water flow ($\approx 0.001H$) in the y direction. The average

5   streamwise velocity, $\langle U \rangle$, for water at $Re_\tau = 840$, polymeric flow (at the same

6   mass flow rate), and the DNS of Hoyas and Jiménez (2008) at $Re_\tau = 934$

7   are compared in Fig. 5 in a semi-logarithmic presentation. The $\langle U \rangle$ profiles

8   for water and polymeric flows are normalized by their corresponding friction

9   velocities, $U^+ = \langle U \rangle / u_\tau$, and shown as functions of wall-normal distance also

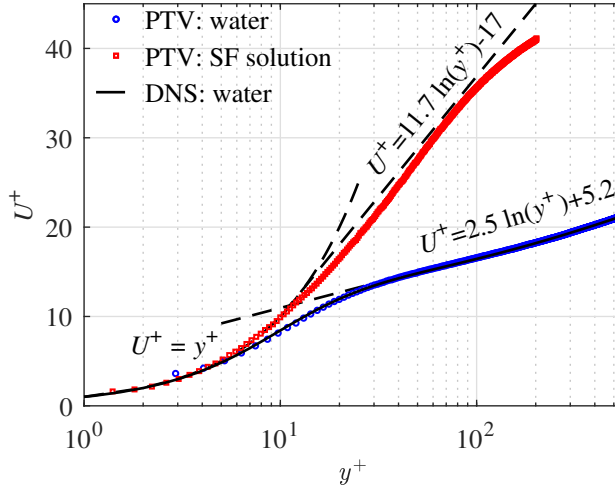10   normalized by the corresponding wall units $y^+ = y/\lambda$. The logarithmic law

Fig. 5: Effect of the SF solution on U^+ profile as a function of y^+. The dashed-lines show $U^+= y^+$, the log-law for Newtonian fluid flows, $U^+= 2.5$ $\ln(y^+)+5.5$, and Virk's asymptote (Virk et al 1970), $U^+= 11.7 \ln(y^+)-17$. The solid line shows the DNS of Hoyas and Jiménez (2008) at $Re_\tau= 934$ for water.

1 of the wall with $\kappa = 0.4$ and $B = 5.2$ is also presented in this figure. The

2 PTV measurement of U^+ for water agrees with the DNS from $y^+ \approx 4$ up to

3 the border of the field of view at $y^+ \approx 550$ in the log-layer, which shows the

4 accuracy of the PTV. The overlap with the log law also indicates the fully

5 developed state of the turbulent channel flow (Bailey et al 2014).

6 The U^+ profile of the polymeric flow follows the $U^+= y^+$ line up to

7 $y^+ \approx 10$. Beyond this location, the profile follows Virk's asymptote (Virk

8 et al 1970) ($U^+= 11.7 \ln(y^+)-17$), which shows that the polymeric flow is at

9 the maximum drag reduction regime. The $DR\%$ of the polymer solution can

10 also be calculated as $DR\% = (1-\tau_\mathrm{w}^\mathrm{p}/\tau_\mathrm{w}^\mathrm{w})\times 100$, where $\tau_\mathrm{w}^\mathrm{w}$ and $\tau_\mathrm{w}^\mathrm{p}$ are the shear

11 stresses of water and the polymeric flows at the wall, estimated from their $\langle U \rangle$

12 profiles, respectively. Based on the $\dot{\gamma}_\mathrm{w}$ and ν_w of water and the polymeric flows

13 (see Table 1), the $\tau_\mathrm{w}^\mathrm{w}$ and $\tau_\mathrm{w}^\mathrm{p}$ are about 10 and 3 Pa, respectively. Therefore,

14 the $DR\%$ of the SF solution based on PTV is about 70%, which is close to

15 $DR\% = 66\%$ obtained from the pressure drop measurement. The polymeric

¹ flow profile deviates from the Virk's asymptote at $y^+ \approx 110$ and follows a

² log law region, which is called "Newtonian plug" (Procaccia et al 2008). This

³ shows that the buffer layer, the region between viscous sublayer and log-layer,

⁴ which starts at $y^+ \approx 10$ ($y/H \approx 0.032$), ends at $y^+ \approx 110$ ($y/H \approx 0.356$) for

⁵ the polymeric flow. The trend of polymeric flow profile in Fig. 5 is consistent

⁶ with the trend of semi-logarithmic U^+-y^+ profile for a polymer solution with

⁷ $DR\%$ of 69% presented by Warholic et al (1999).

⁸   The thickness of the viscous sublayer, the region where $U^+ = y^+$, is about

⁹ $0.006H$ ($y^+ \approx 5$) in water flow, increasing to $0.032H$ ($y^+ \approx 10$) in the

¹⁰ polymeric flow. The buffer layer thickness also increases from about $0.017H$

¹¹ ($\Delta y^+ \approx 15$) in water flow to $0.324H$ ($\Delta y^+ \approx 100$) in the polymeric flow. The

¹² polymer additive also reduces u_τ (see Table 1) and $\langle U \rangle$ near the wall and

¹³ increases $\langle U \rangle$ away from the wall. The reduction of u_τ and increment of $\langle U \rangle$

¹⁴ in the log region shifts the the log-layer profile upward with respect to water

¹⁵ flow, as seen in Fig. 5.

¹⁶   The streamwise, wall-normal, and shear Reynolds stresses ($\langle u^2 \rangle$, $\langle v^2 \rangle$, and

¹⁷ $\langle uv \rangle$, respectively) in unladen Newtonian and non-Newtonian flows are pre-

¹⁸ sented in Fig. 6(a). The Reynolds stresses for both flows are normalized by

¹⁹ friction velocity of the unladen water flow ($u_{\tau 0}$). The wall-normal distance is

²⁰ non-dimensionalized by the wall units of water (λ_0) and polymeric flow (λ_1)

²¹ and presented as y_0^+ and y_1^+ at the lower and upper horizontal axes, respec-

²² tively. The Reynolds stresses for water at $Re_\tau = 840$ are also compared with the

²³ DNS of Newtonian channel flow at $Re_\tau = 934$ by Hoyas and Jiménez (2008).

²⁴ The $\langle u^2 \rangle / u_{\tau 0}^2$ peak for water from 2D-PTV is about 2% lower than the DNS.

²⁵ The maximum magnitudes of $\langle v^2 \rangle / u_{\tau 0}^2$ and $\langle uv \rangle / u_{\tau 0}^2$ are also about 11% and

²⁶ 8% less than the DNS. These differences are associated with the lower Re_τ of

²⁷ the experiment, which causes a thicker inner layer and slightly lower Reynolds
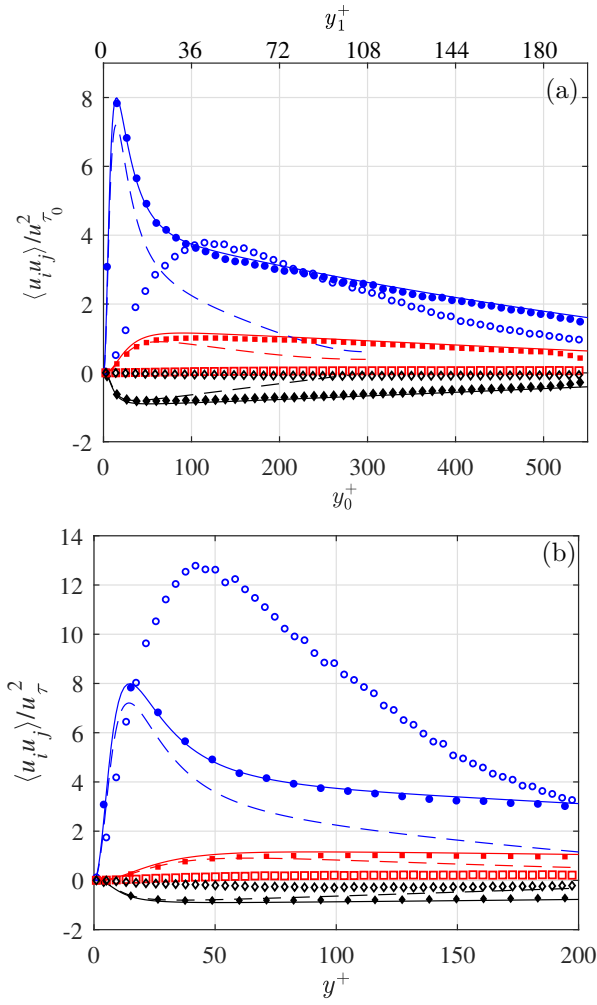
²⁸ stresses.

Fig. 6: Profiles of $\langle u^2 \rangle$ (blue circles), $\langle v^2 \rangle$ (red squares), and $\langle uv \rangle$ (black diamonds) for the Newtonian (filled symbols) and non-Newtonian (open symbols) flows. The profiles are normalized by (a) the inner scaling of water flow and (b) their corresponding inner scaling. Lines show the DNS of Newtonian channel flow at $Re_\tau=934$ by Hoyas and Jiménez (2008) (solid lines) and at $Re_\tau=298$ by Iwamoto et al (2002) (dashed lines). Only one of every ten experimental data points is presented for clarity.

1   As seen in Fig. 6(a), the maximum value of $\langle u^2 \rangle$ of the polymeric flow is

2   about 50% less than that of water. The $\langle v^2 \rangle$ and $\langle uv \rangle$ profiles of the polymeric

3   flow, which almost overlap with each other in Fig. 6(a), are significantly less

than water (almost zero in the measurement domain). The effect of SF solution on the Reynolds stresses is consistent with the results presented by Warholic et al (1999) at high drag reduction regime ($DR\% > 35\%$). At $DR\%$ of 69%, they observed about 40, 85, and 95% reduction in maximum magnitudes of $\langle u^2 \rangle$, $\langle v^2 \rangle$, and $\langle uv \rangle$ profiles, respectively. The measurement also shows that adding the SF polymer to the flow shifts the $\langle u^2 \rangle$ peak away from the wall; the $\langle u^2 \rangle$ profile peaks at $y_0^+ \approx 15$ ($y/H = 0.017$) in water and at $y_0^+ \approx 115$ ($y/H = 0.133$) in the polymeric flow. This is due to a thicker viscous sublayer and buffer layer in the channel flow of the SF solution (Warholic et al 1999, 2001; Mohammadtabar et al 2017).

The Reynolds stresses of unladen Newtonian and non-Newtonian flows are also normalized by their corresponding inner scaling and presented in Fig. 6(b). The polymeric flow has a larger $\langle u^2 \rangle/u_\tau^2$ and smaller $\langle v^2 \rangle/u_\tau^2$ and $\langle uv \rangle/u_\tau^2$ than water, which has a similar flow rate but a higher Re_τ of 840. This trend is consistent with the experimental results of Warholic et al (2001) and DNS results of Dubief et al (2005) at a high drag reduction regime. It is also observed that Reynolds stresses of the polymeric flow at $Re_\tau = 309$ are significantly different than those of DNS of Newtonian turbulent channel flow at similar Re_τ of 298 from Iwamoto et al (2002). This shows that the change in Reynolds stresses of the polymeric flow with respect to the water is not simply due to reduction of Re_τ.

3.2 Bead-laden turbulent flow

The velocity field and the motion of the glass beads in water and the polymeric flows at volumetric concentration of 0.05% are investigated in this section. The wall-normal location and velocity statistics are normalized by the inner scaling of the unladen water flow.

3.2.1 Near-wall number density distribution of the beads

The number density distribution of the beads in the near-wall region of $y <$ $0.64H$ for the water and polymeric flows is presented in Fig. 7. The averaging is carried out using bin size of $2d_{\mathrm{p}}$, and the profiles are normalized by dividing the number of beads in each bin (N) by the average number of beads per bin for water $(\bar{N}_0)$. Normalization using a common value is chosen here to show the effect of the SF solution on the near-wall glass bead concentration. In this analysis, all the bead trajectories are considered without any limitation on trajectory length. As Fig. 7 shows, $N/\bar{N}_0$ increases with reducing y_0^+. This shows that the beads gradually settle in water due to gravity, although turbulence dispersion counteracts and tries to suspend the beads. Since the number of beads in the measurement domain for water is more than the number of beads in the polymeric flow, $N/\bar{N}_0$ is less than one across the measurement domain for the polymeric flow. The suspension of the beads by turbulence in the polymeric flow is expected to be smaller than water flow due to the increase of R (see Table 2) and the negligible $\langle v^2 \rangle$ and $\langle uv \rangle$, as observed in Fig. 6. However, a significant reduction of $N/\bar{N}_0$ is observed in the near-wall region, and the distribution of the beads is more uniform. For beads in the polymeric flow, an increase of $N/\bar{N}_0$ is only observed at $y_1^+ < 36$ $(y < 0.1H)$. The settling velocity of the beads in the polymeric flow is smaller than in the water flow due to the larger μ of the polymer solution. Therefore, based on settling velocity, the beads in the polymeric flow need a longer time and streamwise distance to accumulate in the vicinity of the wall compared with the beads in water flow. It is also important to note that the settling velocity in the polymeric flow depends on local viscosity, which is a function of $\dot{\gamma}$. In the polymeric flow, glass beads settling velocity decreases with an increase of y; therefore, the larger near wall settling velocity has slightly accumulated

the beads at $y_0^+ < 100$. This observation also shows that, in polymer drag

reduced flows, although turbulence dispersion is small, inertial particles may

not accumulate in the near-wall region due to their smaller settling velocity

when they are away from the wall. In addition, using DNS, Huang et al (1997)

showed that the inertial particles in viscoelastic fluids tend to move away from

the wall. They showed that when $\beta = d_{\mathrm{p}}/(2H)$ is small (β was 0.025 in their

study while it is 0.017 in the current study) particles tend to move toward the

region with lower $\dot{\gamma}$ due to normal stresses of the viscoelastic fluid, which are

induced by the gradient of the velocity profile.

The important observation here is the small concentration of the beads

near the lower wall of the channel, which reduces the probability for collision

of the beads with the wall in the polymeric flow. This suggests a smaller wear

rate and energy loss in particle-laden flows with drag-reducing polymers. To

the authors' knowledge, the reduction of particle concentration in the near-wall

region of viscoelastic flows, and their migration toward the center of channel,

were only reported in microchannels, and for laminar or transitional flows

(Yang et al 2011; Kang et al 2013; Lim et al 2014; Huang et al 1997; Di Carlo

et al 2007; Leshansky et al 2007; D'Avino et al 2012; Del Giudice et al 2013;

Ciftlik et al 2013).

3.2.2 Average streamwise velocity of the beads

The profiles of $\langle U \rangle$ for the fluid and beads in water and polymeric flows are

normalized by $u_{\tau 0}$, and presented as $U_0^+ = \langle U \rangle / u_{\tau 0}$ in Fig. 8. For the first data

point, which corresponds to an averaging bin from the wall up to $y^+ = 28.8$,

the beads velocity in water is larger than the velocity of the unladen water.

This larger velocity of the beads at the wall is because the no-slip boundary

condition does not apply to them; beads can slide or roll on the wall. In the

log layer ($y_0^+ > 30$), the U_0^+ of the beads is less than the unladen water flow,
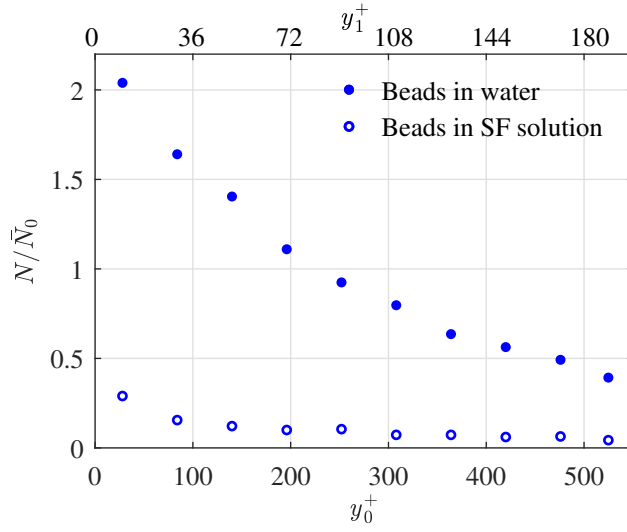
Fig. 7: The effect of SF solution on the number density distribution of the beads.

1 which is due to the higher inertia of the beads (Shokri et al 2017; Ahmadi et al

2 2019).

3 The U_0^+ profile of the unladen polymer solution is lower than U_0^+ of water

4 at $y_0^+ < 300$ ($y/H < 0.348$). This wall-normal range extends to the border of

5 the buffer layer for the polymeric flow. Since the beads absorb their kinematic

6 energy from the carrier phase, the beads also have a smaller velocity in this

7 region. The smaller beads velocity at the near wall reduces the momentum

8 exchange and the tangential force that is exerted on the wall during their

9 collision with the wall. In the viscous sublayer, and most of the buffer layer of

10 the polymeric flow, the velocity of the beads is slightly larger than its unladen

11 counterpart.

12 *3.2.3 Reynolds stresses of the beads*

13 The effect of the polymer solution on the Reynolds stresses of the beads is

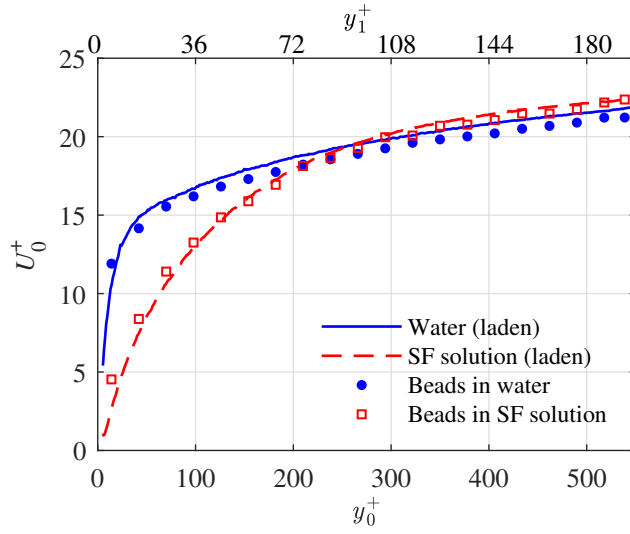14 shown in Fig. 9, obtained by averaging PTV data using $2d_\mathrm{p}$ bin size. The

Fig. 8: Effect of the polymeric flow on the average streamwise velocity profile of the beads. The lines show the normalized average streamwise velocity of the fluid in the bead-laden flows.

1 $\langle u^2 \rangle$ profile of the beads in water is maximum at the first bin ($y_0^+ = 14.4$),

2 where the maximum value of $\langle u^2 \rangle$ of the unladen water flow was observed in

3 Fig. 6. As Fig. 9 shows, the effect of the polymer solution on $\langle u^2 \rangle$ is smaller

4 than its effect on $\langle v^2 \rangle$ and $\langle uv \rangle$. This is similar to the effect of the SF solution

5 on the $\langle v^2 \rangle$ and $\langle uv \rangle$ profiles of the unladen flow (see Fig. 6). The reduction

6 of $\langle uv \rangle$ of the beads shows weaker sweep and ejection motions, which are

7 the major mechanisms for wall-normal dispersion of the beads (Kiger and

8 Pan 2002). Therefore, the trajectory of the beads in the polymeric flow are

9 relatively aligned in the streamwise direction. This is observed in the sample

10 bead trajectories in polymer solution and water in Fig. 4; the trajectories of the

11 beads in the polymer solution has a smaller displacement in the wall-normal

12 direction. This is expected to reduce the impact angle and collision probability

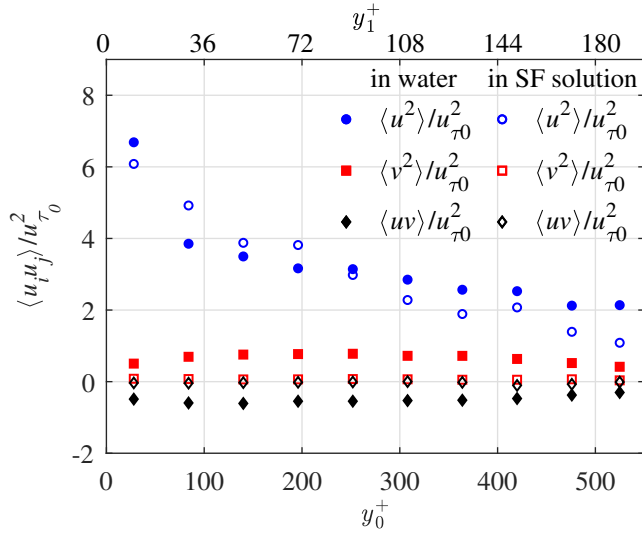13 of the beads with the channel wall.

Fig. 9: Reynolds stresses of the beads in the water and polymeric flow.

1 *3.2.4 Near-wall motion of the beads*

2 The effect of the polymeric flow on the motion of the inertial beads is inves-

3 tigated here by applying conditional averaging on their instantaneous wall-

4 normal velocity (V). In the discussion, we refer to the beads moving toward

5 the bottom wall ($V < 0$) as downward moving beads, and the beads moving

6 toward the center of the channel ($V > 0$) as upward moving beads. The wall-

7 normal velocity of the beads is conditionally averaged based on the V sign

8 (i.e. their motion toward or away from the wall) for the water and polymeric

9 flow. The result is normalized by $u_{\tau 0}$ ($V_0^+ = \langle V \rangle / u_{\tau 0}$) and presented in Fig.

10 10. The V_0^+ of the beads in the polymer solution, in terms of both upward and

11 downward motions, is significantly smaller than their velocity in water. The

12 SF solution reduces V_0^+ of the beads with downward motion at $y_0^+ = 14.4$ by

13 about 80%, which is also expected to reduce the wall-collision probability.

14   The average of the velocity vector magnitude in $x - y$ plane ($|\overrightarrow{V}|$) for the

15 upward and downward moving beads is presented in Fig. 11 to investigate
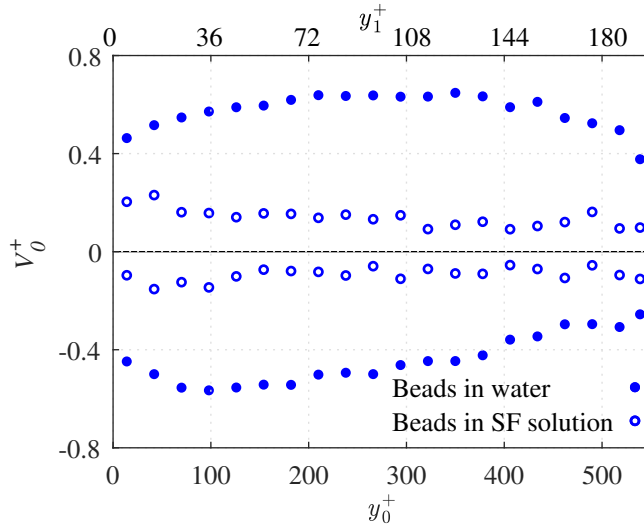
Fig. 10: Effect of the SF solution on V_0^+ of the beads with upward and downward motions.

1   their momentum. It is observed that the momentum of the beads at $y_0^+ = 14.4$

2   is reduced by about 60% in the polymeric flow compared with water flow. The

3   reduction of the beads momentum near the wall reduces the collision force

4   upon impact with the wall. In water flow, the $|\overrightarrow{V}|$ of downward moving beads

5   is greater than that of the upward moving beads by about $1.2u_{\tau 0}$. This is

6   because the downward moving beads move from a region with a larger $\langle U \rangle$ to

7   a region with a smaller $\langle U \rangle$, transporting the momentum toward the wall. The

8   difference between $|\overrightarrow{V}|$ of downward and upward moving beads also exists in

9   the polymeric flow but it is smaller than the water flow. This is associated

10 with the smaller wall-normal velocity and therefore their smaller wall-normal

11 transport in the polymeric flow.

12   The motion of the beads is also characterized here using their trajectory

13 angle, $\theta = \tan^{-1}(V/U)$. A downward moving bead has $\theta < 0$ ($V < 0$, $U > 0$)

14 and an upward moving bead has $\theta > 0$ ($V > 0$, $U > 0$). The trajectory angle

15 for the beads is useful for modeling wall-collision and evaluation of numerical
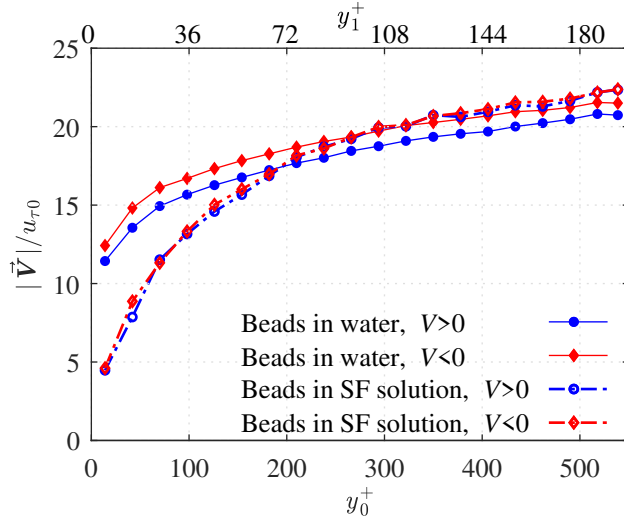
Fig. 11: The average velocity of the beads with upward or downward motion in water and polymeric flows.

simulations of two-phase turbulent channel flows. The trajectory angles of the beads in water and polymeric flows are conditionally averaged based on the sign of V and is presented in Fig. 12. This figure shows that the average trajectory angle of the beads, $\langle\theta\rangle$, for the downward and upward moving beads in water flow is $\langle\theta\rangle = -2.3°$ and $2.3°$ in the immediate vicinity of the wall at $y_0^+ = 14.4$. In the polymeric flow, these angles are smaller and equal to $-1.2°$ and $2.6°$ for downward and upward beads, respectively. In general, the trajectory angle of the beads in the polymeric flow is significantly smaller than in the water except for the upward beads at $y_0^+ \approx 14.4$. The smaller trajectory angle for the beads in the polymeric flow is consistent with the previous observation of small wall-normal velocity in Fig. 9 and Fig. 10. The $\langle\theta\rangle$ of downward beads at $y_0^+ \approx 14.4$ is reduced by about 45% in the polymeric flow compared with water. This is important in terms of bead-wall collision; the reduction of the impact angle of the beads with the wall, along with the

₁ reduction of their momentum (see Fig. 11) can potentially reduce pipe wear
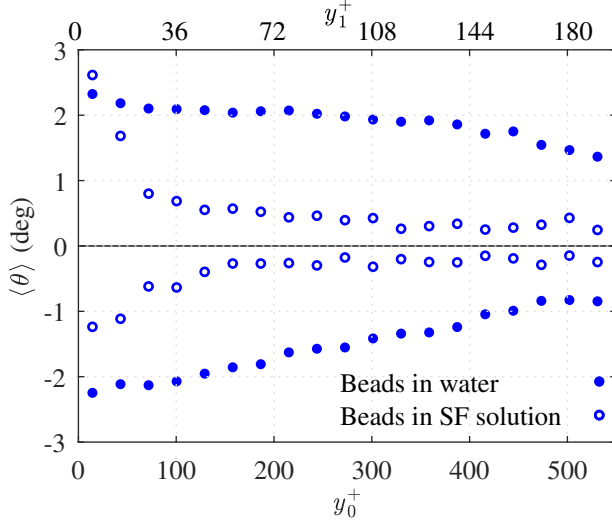
₂ rate in two-phase systems.

Fig. 12: The average trajectory angle of the beads with upward or downward motion.

₃   A quadrant analysis of turbulent fluctuations is carried out to investigate

₄ the effect of the SF solution on the ejection and sweep motions of the beads

₅ (Wallace 2016). Joint probability density function (JPDF) of velocity fluctua-

₆ tions for the unladen and laden flows of water and SF solution in three different

₇ wall-normal locations is presented in Fig. 13. The selected locations include

₈ $y_0^+ \approx 14.4$, which is at the center of the first bin immediately after the wall,

₉ $y_0^+ \approx 100$, the location of maximum $\langle u^2 \rangle$ for the unladen SF solution, and

₁₀ $y_0^+ \approx 530$, which is the farthest available data point from the lower channel

₁₁ wall. Each JPDF has four quadrants associated with four different turbulent

₁₂ motions: upward interaction (quadrant 1; $u > 0$, $v > 0$); ejection (quadrant 2;

₁₃ $u < 0$, $v > 0$); downward interaction (quadrant 3; $u < 0$, $v < 0$); and sweep

₁₄ (quadrant 4; $u > 0$, $v < 0$) (Wallace et al 1972). The total JPDF percentage

of each quadrant is also indicated at the corner of each quadrant. In all the plots of Fig. 13, u and v are normalized by $u_{\tau 0}$.

Comparing the results for unladen water and polymeric flows in the first and second rows of Fig. 13 shows that the ejection and sweep motions are weaker in the polymeric flow. For example, ejection and sweep motions in the unladen water flow at $y_0^+ \approx 14.4$ (Fig. 13(a)) are dominant compared with the other quarters and each forms 34% of the motion. However, their contribution in the polymeric flow is smaller, as seen in Fig. 13(d); ejections form 28% and sweeps form 24% of the motions, similar to the other quadrants. There is also no evidence of strong ejection and sweep motions (large u and v) in Fig. 13(d, e, and f).

The sweep and ejection motions also dominate the turbulent motions of the beads at $y_0^+ \approx 14.4$ and 100 (see plots (g) and (h) in Fig. 13), which is consistent with Fig. 13(a) and (b). However, away from the wall at $y_0^+ \approx 530$, sweep and ejection motions of the beads are weaker and the beads mostly move downward (3rd and 4th quadrants) due to gravity, as seen in Fig. 13(i). The JPDF contour of the beads in the polymeric flow (4th row of Fig. 13) shows different behavior compared with the beads in water. At $y_0^+ \approx 14.4$, a large number of beads in the polymer solution have a downward motion, as seen by the greater JPDF of the 3rd and 4th quadrants of Fig. 13(j). This is because the ejection motion, which is the main mechanism to suspend the beads away from the wall, is weak in the polymeric flow and the beads motion is dominated by a downward fluctuation due the effect of gravity. At $y_0^+ \approx 100$ and 530, the trend is opposite and more beads have $v > 0$ in Fig. 13(k) and (l). The upward motion is associated with the normal stress of the viscoelastic fluids (Huang et al 1997). Therefore, the quadrant analysis shows that the sweep and ejections are not the major mechanism for wall-normal dispersion of the beads in the polymeric flow.
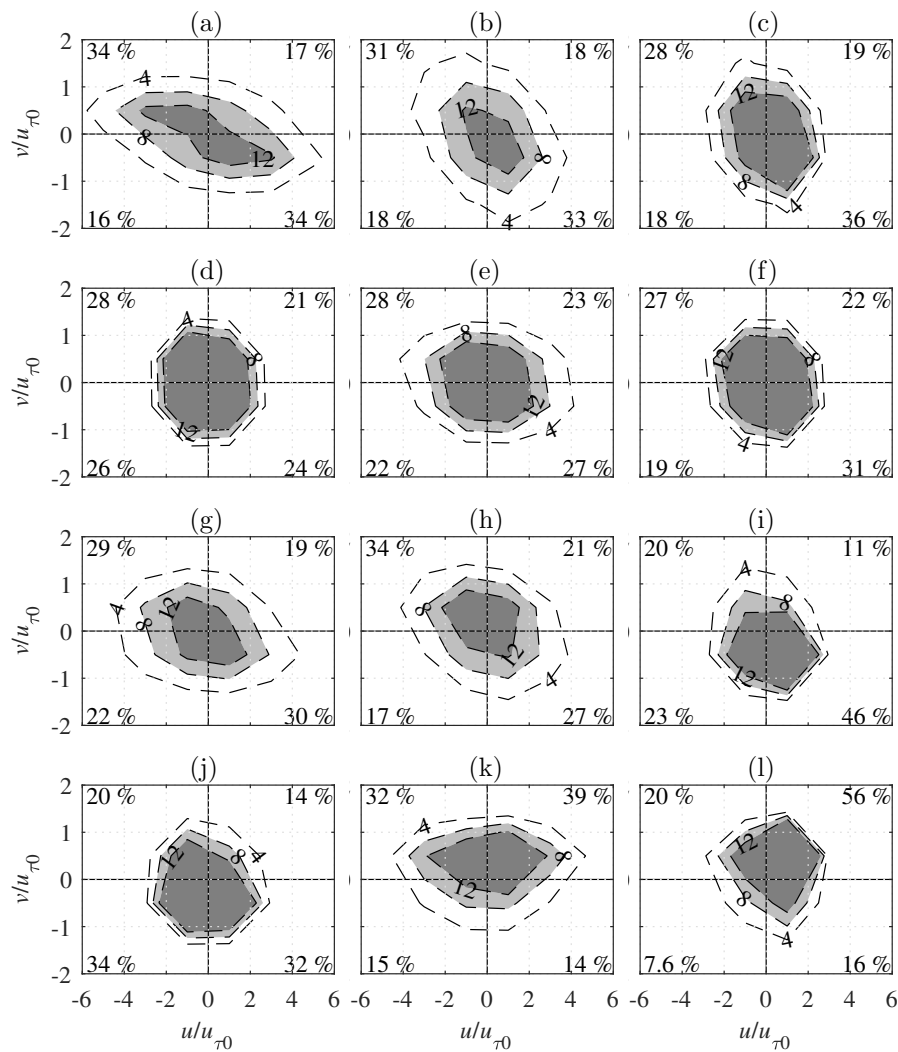
Fig. 13: Joint probability density function of normalized velocity fluctuations of unladen water flow (a, b, and c), unladen polymeric flow (d, e, and f), beads in water flow (g, h, and i), and beads in polymeric flow (j, k, and l). The plots in each row correspond to $y_0^+ \approx 14.4$, 100, and 530, from left to right, respectively. The number at the corners of each plot shows the percentage of turbulent motions in the associated quarter. The number on each contour shows the JPDF percentage.

4 Conclusion

We investigated the motion of 250 μm glass beads with volumetric concentration of 0.05% in a turbulent flow of drag-reduced polymer solution using time-resolved particle tracking velocimetry. A 90 ppm solution of Superfloc (SF) polymer in water with about 66% drag reduction was used as the drag reducing polymer solution. Experiments were carried out at mass flow rate of 3.66 kg/s for water and the polymer solution, which was equivalent to Reynolds number of 34,300, based on bulk velocity, height of the channel, and the kinematic viscosity of water. Results showed that the SF solution reduced the number density of the beads and distributed them more evenly, near the channel lower wall, in the wall-normal direction. The SF solution also reduced the average streamwise velocity, $\langle U \rangle$, of the beads close to the wall and increased it away from the wall relative to the $\langle U \rangle$ profile of the beads in water flow. The addition of the polymer to the carrier phase did not change the streamwise Reynolds stress of the beads but it significantly reduced wall-normal and shear Reynolds stresses of the beads. In addition, the average wall-normal velocity of the beads reduced and their trajectory became more aligned with streamwise direction in the polymeric flow. The momentum of the beads in the immediate vicinity of the wall in polymeric flow was about 60% smaller than in the water flow. The quadrant analysis of beads motion showed that ejection and sweep motions of the beads were attenuated in the polymeric flow and were not a major mechanism for wall-normal dispersion of the beads. The reduction of the number density, trajectory angle with respect to the wall, and the momentum of the beads near the channel wall in the polymeric flow indicate the potential of drag-reducing polymers for reducing erosion wear in slurry pipes.

Appendix

The random error of velocity statistics of unladen and bead-laden flows are determined based on the statistical convergence of the last 20% of data collected at $y_0^+ = 14.4$ and are presented in Table 4.

Table 4: The random error of the average velocity and Reynolds stresses of unladen and bead-laden flows based on the statistical convergence of the last 20% of data collected at $y_0^+ = 14.4$.

Random error	$\langle U \rangle$ $\times 10^3$ m/s	$\langle V \rangle$ $\times 10^4$ m/s	$\langle u^2 \rangle$ $\times 10^3$ (m/s)^2	$\langle v^2 \rangle$ $\times 10^5$ (m/s)^2	$\langle uv \rangle$ $\times 10^5$ (m/s)^2
Unladen water flow	0.86	0.52	0.10	1.20	0.48
Unladen polymeric flow	0.55	0.05	0.03	0.23	0.15
Beads in laden water flow	4.10	4.00	0.70	5.20	8.00
Beads in laden polymeric flow	5.20	2.60	3.80	4.10	7.50

References

Ahmadi F, Ebrahimian M, Sanders RS, Ghaemi S (2019) Particle image and tracking velocimetry of solid-liquid turbulence in a horizontal channel flow. Int J Multiphase Flow 112:83–99

Arnipally SK, Kuru E (2017) Settling velocity of particles in viscoelastic fluids: a comparison of the shear viscosity vs elasticity effect. SPE J 23, DOI 10.2118/187255-PA

Atherton TJ, Kerbyson DJ (1999) Size invariant circle detection. Image Vision Comput 17(11):795–803

Bailey S, Vallikivi M, Hultmark M, Smits A (2014) Estimating the value of von kármán's constant in turbulent pipe flow. J Fluid Mech 749:79–98

Chhabra R (2006) Bubbles, drops, and particles in non-Newtonian fluids. CRC press

Chhabra R, Richardson J (1999) Non-Newtonian flow in the process industries. Butterworth-Heinemann

Ciftlik A, Ettori M, Gijs M (2013) High throughput-per-footprint inertial focusing. Small 9(16):2764–2773

Clift R, Gauvin W (1971) Motion of entrained particles in gas streams. CAN J Chem Eng 49(4):439–448

Corredor F, Bizhani M, Kuru E (2015) Experimental investigation of drag reducing fluid flow in annular geometry using particle image velocimetry technique. J Fluids Eng 137(8):081103

D'Avino G, Maffettone P (2015) Particle dynamics in viscoelastic liquids. J Non-Newton Fluid 215:80–104

D'Avino G, Romeo G, Villone M, Greco F, Netti P, Maffettone P (2012) Single line particle focusing induced by viscoelasticity of the suspending liquid: theory, experiments and simulations to design a micropipe flow-focuser. Lab on a Chip 12(9):1638–1645

Del Giudice F, Romeo G, D'Avino G, Greco F, Netti PA, Maffettone P (2013) Particle alignment in a viscoelastic liquid flowing in a square-shaped microchannel. Lab on a Chip 13(21):4263–4271

Di Carlo D, Irimia D, Tompkins R, Toner M (2007) Continuous inertial focusing, ordering, and separation of particles in microchannels. P Natl A Sci USA 104(48):18892–18897

Dubief Y, White C, Terrapon V, Shaqfeh E, Moin P, Lele S (2004) On the coherent drag-reducing and turbulence-enhancing behaviour of polymers in wall flows. J Fluid Mech 514:271–280

Dubief Y, Terrapon V, White C, Shaqfeh E, Moin P, Lele S (2005) New answers on the interaction between polymers and vortices in turbulent flows. Flow Turb Combust 74(4):311–329

Einstein A (1956) Investigations on the theory of the Brownian movement. Courier Corporation

Gauthier F, Goldsmith H, Mason S (1971) Particle motions in non-newtonian media. II. Poiseuille flow. T Soc Rheol 15(2):297–330

Gerashchenko S, Sharp N, Neuscamman S, Warhaft Z (2008) Lagrangian measurements of inertial particle accelerations in a turbulent boundary layer. J Fluid Mech 617:255–281

Gupta R, Singh S, Sehadri V (1995) Prediction of uneven wear in a slurry pipeline on the basis of measurements in a pot tester. Wear 184(2):169–178

Hatschek E (1939) An introduction to industrial rheology. by GW Scott Blair. J Phys Chem 43(3):395–395

Hoyas S, Jiménez J (2008) Reynolds number effects on the Reynolds-stress budgets in turbulent channels. Phys Fluids 20(10):101511

Huang PY, Feng J, Hu HH, Joseph DD (1997) Direct simulation of the motion of solid particles in couette and poiseuille flows of viscoelastic fluids. J Fluid Mech 343:73–94

Iwamoto K, Suzuki Y, Kasagi N (2002) Reynolds number effect on wall turbulence: toward effective feedback control. Int J Heat Fluid Flow 23(5):678–689

Joseph GG, Zenit R, Hunt ML, Rosenwinkel AM (2001) Particle–wall collisions in a viscous fluid. J Fluid Mech 433:329–346

Kaftori D, Hetsroni G, Banerjee S (1995a) Particle behavior in the turbulent boundary layer. I. motion, deposition, and entrainment. Physics of Fluids 7(5):1095–1106

Kaftori D, Hetsroni G, Banerjee S (1995b) Particle behavior in the turbulent boundary layer. II. velocity and distribution profiles. Phys Fluids 7(5):1107–1121

Kähler CJ, Scharnowski S, Cierpka C (2012) On the uncertainty of digital PIV and PTV near walls. Exp Fluids 52(6):1641–1656

Kang K, Lee SS, Hyun K, Lee SJ, Kim JM (2013) DNA-based highly tunable particle focuser. Nat Commun 4:2567

Karabelas AJ (1978) An experimental study of pipe erosion by turbulent slurry flow. Proc HT5 pp 47–61

Karniadakis GE, Choi K (2003) Mechanisms on transverse motions in turbulent wall flows. Annu Rev Fluid Mech 35(1):45–62

Karnis A, Mason SG (1966) Particle motions in sheared suspensions. xix. viscoelastic media. T Soc Rheol 10(2):571–592

Kaushal D, Sato K, Toyota T, Funatsu K, Tomita Y (2005) Effect of particle size distribution on pressure drop and concentration profile in pipeline flow of highly concentrated slurry. Int J Multiphase Flow 31(7):809–823

Kiger KT, Pan C (2002) Suspension and turbulence modification effects of solid particulates on a horizontal turbulent channel flow. J Turbul 3(19):1–17

Kim K, Li CF, Sureshkumar R, Balachandar S, Adrian RJ (2007) Effects of polymer stresses on eddy structures in drag-reduced turbulent channel flow. J Fluid Mech 584:281–299

Kosel TH (1992) Solid particle erosion. ASM handbook 18:199–213

Leshansky AM, Bransky A, Korin N, Dinnar U (2007) Tunable nonlinear viscoelastic focusing in a microfluidic device. Phys Rev Lett 98(23):234501

Li G, McKinley GH, Ardekani AM (2015) Dynamics of particle migration in channel flow of viscoelastic fluids. J Fluid Mech 785:486–505

Lim EJ, Ober TJ, Edd JF, Desai SP, Neal D, Bong KW, Doyle PS, McKinley GH, Toner M (2014) Inertio-elastic focusing of bioparticles in microchannels at high throughput. Nature Commun 5:4120

Luchik TS, Tiederman WG (1988) Turbulent structure in low-concentration drag-reducing channel flows. J Fluid Mech 190:241–263

Marchioli C, Soldati A (2002) Mechanisms for particle transfer and segregation in a turbulent boundary layer. J Fluid Mech 468:283–315

McKinley GH (2002) Steady and transient motion of spherical particles in viscoelastic liquids. In: Kee DD, Chhabra RP (eds) Transport Processes in Bubble, Drops, and Particles, New York: Taylor & Francis, pp 338–375

Mishra S AA Chandra H (2012) Solid liquid non-Newtonian fluid flow in pipe: a review. Acta Mech Slovaca 16(2):62–73

Mohammadtabar M, Sanders RS, Ghaemi S (2017) Turbulent structures of non-newtonian solutions containing rigid polymers. Phys Fluids 29(10):103101

Morgado WAM, Oppenheim I (1997) Energy dissipation for quasielastic granular particle collisions. Phys Rev E 55:1940–1945, DOI 10.1103/PhysRevE. 55.1940

Ohmi K, Li H (2000) Particle-tracking velocimetry with new algorithms. Meas Sci Tech 11(6):603

Pedinotti S, Mariotti G, Banerjee S (1992) Direct numerical simulation of particle behaviour in the wall region of turbulent flows in horizontal channels. Int J of Multiphase Flow 18(6):927–941

Procaccia I, L'vov VS, Benzi R (2008) Colloquium: Theory of drag reduction by polymers in wall-bounded turbulence. Rev Modern Phys 80(1):225

Rouse H (1937) Modern conceptions of the mechanics of fluid turbulence. T A Soc Civ Eng 102:463—-554

Rowin WA, Sanders RS, Ghaemi S (2018) A recipe for optimum mixing of polymer drag reducers. J Fluids Eng 140(11):111402

Senapati PK, Mishra BK, Parida A (2010) Modeling of viscosity for power plant ash slurry at higher concentrations: Effect of solids volume fraction, particle size and hydrodynamic interactions. Powder Tech 197(1-2):1–8

Seo KW, Kang YJ, Lee SJ (2014) Lateral migration and focusing of microspheres in a microchannel flow of viscoelastic fluids. Phys Fluids 26(6):063301

Shokri R, Ghaemi S, Nobes DS, Sanders RS (2017) Investigation of particle-laden turbulent pipe flow at high-reynolds-number using particle image/tracking velocimetry (PIV/PTV). Int J Multiphase Flow 89:136–149

Soldati A (2005) Particles turbulence interactions in boundary layers. ZAMM-Journal of Applied Mathematics and Mechanics/Zeitschrift für Angewandte Mathematik und Mechanik 85(10):683–699

Soldati A, Marchioli C (2009) Physics and modelling of turbulent particle deposition and entrainment: Review of a systematic study. Int J Multiphase Flow 35(9):827–839

Stickel JJ, Powell RL (2005) Fluid mechanics and rheology of dense suspensions. Annu Rev Fluid Mech 37:129–149

Sumer BM, Deigaard R (1981) Particle motions near the bottom in turbulent flow in an open channel. Part 2. J Fluid Mech 109:311–337

Tatterson GB (1991) Fluid mixing and gas dispersion in agitated tanks. McGraw-Hill Companies

Taylor GI (1923) Stability of a viscous liquid contained between two rotating cylinders. Phil Trans R Soc London 223:289–343

Virk PS, Mickley HS, Smith KA (1970) The ultimate asymptote and mean flow structure in toms' phenomenon. J Appl Mech 37(2):488–493

Voth GA, la Porta A, Crawford AM, Alexander J, Bodenschatz E (2002) Measurement of particle accelerations in fully developed turbulence. J Fluid Mech 469:121–160

Wallace JM (2016) Quadrant analysis in turbulence research: history and evolution. Annu Rev Fluid Mech 48:131–158

Wallace JM, Eckelmann H, Brodkey RS (1972) The wall region in turbulent shear flow. J Fluid Mech 54(1):39–48

Warholic MD, Massah H, Hanratty TJ (1999) Influence of drag-reducing polymers on turbulence: effects of reynolds number, concentration and mixing. Exp Fluids 27(5):461–472

Warholic MD, Heist DK, Katcher M, Hanratty TJ (2001) A study with particle-image velocimetry of the influence of drag-reducing polymers on the structure of turbulence. Exp Fluids 31(5):474–483

Wasp EJ, Kenny JP, Gandhi RL (1977) Solid–liquid flow: slurry pipeline transportation. [pumps, valves, mechanical equipment, economics]. Ser Bulk Mater Handl; (USA) 1:4

White CM, Mungal MG (2008) Mechanics and prediction of turbulent drag reduction with polymer additives. Annu Rev Fluid Mech 40:235–256

White CM, Somandepalli VSR, Mungal MG (2004) The turbulence structure of drag-reduced boundary layer flow. Exp Fluids 36(1):62–69

Yang S, Kim JY, Lee SJ, Lee SS, Kim JM (2011) Sheathless elasto-inertial particle focusing and continuous separation in a straight rectangular microchannel. Lab on a Chip 11(2):266–273

Yuen HK, Princen J, Illingworth J, Kittler J (1990) Comparative study of Hough transform methods for circle finding. Image Vision Comput 8(1):71–77